Check for updates

Advanced Energy Materials

ADVANCED ENERGY MATERIALS
www.advenergymat.de

RESEARCH ARTICLE

Solar Salt Thermal Storage Enhancement Through Defect Engineering

Chang Ji[1] | Xueming Yang[1] | Qiyang Cui[1] | Xudong Zhang[2] | Jianfei Xie[3] | Bingyang Cao[4]

[1]Hebei Key Laboratory of Energy Storage and Integrated Energy Systems, Department of Power Engineering, North China Electric Power University, Baoding, People's Republic of China | [2]State Key Laboratory of Cryogenic Science and Technology, Technical Institute of Physics and Chemistry, Chinese Academy of Sciences, Beijing, People's Republic of China | [3]School of Engineering, University of Derby, Derby, United Kingdom | [4]Key Laboratory for Thermal Science and Power Engineering of Ministry of Education, Department of Engineering Mechanics, Tsinghua University, Beijing, People's Republic of China

Correspondence: Xueming Yang (xuemingyang@ncepu.edu.cn) | Xudong Zhang (xdzhang@mail.ipc.ac.cn) | Bingyang Cao (caoby@tsinghua.edu.cn)

Received: 10 June 2026 | **Revised:** 24 August 2026 | **Accepted:** 8 September 2026

Keywords: concentrated solar power | heat capacity | molten salt | nanofluid | nanoparticle | thermal conductivity | thermal energy storage | vacancy defect

ABSTRACT

Molten salts nanofluids-based thermal energy storage systems offer a viable solution for the advancing of concentrated solar power (CSP) systems and grid peak shaving. However, further enhancement of the thermal energy storage performance of molten salts nanofluids is facing a bottleneck. Here, we report a novel defect-engineering method that can overcome this obstacle by incorporating the oxygen vacancy (Vo) into silica nanoparticles dispersed in solar salts. By integrating experiments, DFT-based charge analysis, MD simulations, and techno-economic analysis, solar salt thermal storage enhancement through defect engineering is systematically investigated from microscale to system level. Unlike SiO_2 nanoparticles without V_O, V_O-engineered SiO_2 nanoparticles induce strong Coulombic interactions with molten salt ions, which can reorganize the molten salt ions into an exceptionally dense and thick compressed layer. This unique structure triples the specific heat capacity enhancement achievable with conventional nanoparticle doping, yielding a maximum increase of 56.6%. Concurrently, the thermal conductivity, dispersibility, and viscosity have also been significantly improved. System-level analysis reveals that these integrated thermophysical enhancements directly reduce the levelized cost of electricity and increase the annual energy generation of CSP system. The established oxygen vacancy engineering provides a novel approach to underpin the potential of molten salts nanofluids-based thermal energy storage.

1 | Introduction

The low-carbon energy revolution relies on the deployment of large-scale, long-duration, and cost-effective energy storage technologies [1–4]. Thermal energy storage (TES), particularly the high-temperature sensible heat storage using molten salts, plays a crucial role in concentrated solar power (CSP) system, grid peak shaving, industrial waste heat recovery, and clean heating [5]. However, its widespread application is constrained by the relatively low thermal energy storage density of molten salt media. Since the sensible heat storage capacity of molten salts is governed by the product of the specific heat capacity (c_p) and the temperature rise, while the practical temperature rise in thermal energy storage systems is already close to the allowable limits of structural materials, enhancing the c_p of molten salts has emerged as the central scientific challenge in molten salt thermal energy storage [6]. Addressing this challenge is vital toward maximizing the system energy density, reducing the storage volume and costs, and ultimately improving the techno-economic viability and safety of molten-salt thermal energy storage technology.

All rights reserved, including rights for text and data mining and training of artificial intelligence technologies or similar technologies.
© 2026 Wiley-VCH GmbH

The thermophysical properties of molten salts can be optimized by tailoring the multi-component eutectic compositions [7]; once the salt composition is fixed, further enhancement is mainly achieved through nanoparticle doping, which has been reported to improve c_p and thermal conductivity, either individually or simultaneously, in molten salt systems [8–10]. This strategy exploits the high specific surface area of nanoparticles to induce the interfacial effects that can help improve c_p. This interfacial effect of tracing amounts of nanoparticles is commonly attributed to the "compressed layer" mechanism, whereby interactions between the dispersed nanoparticles and surrounding ions lead to an interfacial layer with higher ion concentration and a more ordered ionic arrangement than in the bulk molten salt. The resulting compressed layer exhibits higher ionic density than the bulk liquid and shows properties distinct from those of the bulk liquid, thereby contributing to the obvious increase in c_p [11, 12]. However, the limited performance gains achieved by these strategies are accompanied by a few drawbacks, such as the nanoparticle agglomeration and sedimentation during long-term cycling, as well as the increased viscosity and degraded heat transfer performance [13, 14]. Consequently, developing stable and effective molten salt nanofluids to substantially enhance their c_p is still challenging.

Among the commonly used nanoparticles, SiO_2 has been extensively investigated in molten-salt nanofluids because of its relatively low cost, chemical stability, and compatibility with nitrate salts [15, 16]. Some studies have attempted to enhance the thermal energy storage performance of molten salts by introducing functional groups on nanoparticle surfaces to regulate the interfacial ion adsorption through Coulombic interactions [17, 18]. For instance, Wen et al. [19] combined molecular dynamics (MD) simulations with experiments, showing that the surface-hydroxylated SiO_2 can template an ordered interfacial ion arrangement, increase the interfacial electrostatic potential energy and local thermal expansion coefficient, and enhance the c_p up to 19%. However, the density of surface hydroxyl groups on SiO_2 has been reportedly reduced to approximately 38% of its initial value when the temperature reaches 500°C [20], suggesting a thermal-stability limitation of this organic functional group surface modification strategy in high-temperature molten salt environments. One should note that most of the existing studies on enhanced c_p have only been focused on nanoparticle doping without treatment. Research on the effect of surface modifications of oxide nanoparticles on thermal energy storage performance of molten salt is still rare and at an initial exploration stage, thus requiring considerable exploration. In fact, further enhancement of the thermal energy storage performance of molten salts nanofluids faces a bottleneck.

Here, we report a novel defect-engineering method that can overcome this obstacle by incorporating the oxygen vacancy (Vo) into SiO_2 nanoparticles dispersed in solar salts. Introducing surface defects for nanoparticles can modulate the charge distributions and strengthen the interaction between the molten salts and nanoparticles, helping enhance the thermal energy capability of the molten salt nanofluids. Compared to surface functionalization, this approach offers superior thermal stability in high-temperature environments [21]. In this work, we combine experimental characterization and MD simulations to elucidate the interfacial behavior of Vo-molten salt nanofluids (V_O-MSNFs). It has been found that the introduction of V_O-engineered SiO_2 nanoparticles enlarges the Coulombic interactions at the interface, which promote the formation of denser and thicker ionic compression layers. This structural reorganization leads to a remarkable increase of 56.6% in c_p of V_O-MSNF compared to solar salts. Moreover, the dispersion stability and transport properties of V_O-MSNF have been evaluated, and the levelized cost of electricity (LCOE) and annual energy generation (AEG) of CSP systems employing V_O-MSNF have been quantitatively assessed. The proposed method establishes V_O engineering as an effective route for regulating the nanoparticle-salt interface, examines the associated enhancement mechanism in terms of electrostatic interactions, and demonstrates its potential to improve the thermophysical performance of solar salt nanofluids and CSP systems.

The rest of this paper is organized as follows. Section 2.1 presents the preparation and specific heat capacity enhancement of V_O-MSNF. Section 2.2 elucidates the defect-induced interfacial ionic structure and the corresponding heat capacity enhancement mechanism. Sections 2.3 and 2.4 evaluate the thermal and dispersion stability, thermal conductivity, and viscosity of V_O-MSNF. Section 2.5 assesses its potential benefits at the TES component and CSP system levels through techno-economic analysis. Finally, Sections 3 and 4 present the conclusions and methods, respectively.

2 | Results and Discussion

2.1 | Synthesis and Heat Capacity of V_O-MSNF

In this study, the preparation process of the molten salt nanofluid V_O-engineered SiO_2 nanoparticles is shown in Figure 1a. SiO_2 nanoparticles with V_O were obtained by annealing the untreated SiO_2 nanoparticles in a tube furnace under a nitrogen atmosphere condition at 1150°C for 5–8 h, followed by natural cooling under N_2. Previous studies [22, 23] about Si basic physical science have shown that high-temperature annealing of SiO_2 at 1150°C in N_2 can induce oxygen-deficient regions. At this temperature, Si—O bonds can be cleaved near pre-existing point defects, followed by the outward diffusion of released oxygen. In addition, E′-type defects have been experimentally observed in nanosized SiO_2 and shown to evolve during high-temperature treatment under low oxygen partial pressure [24]. The obtained SiO_2 nanoparticles with V_O were subsequently mixed with a binary eutectic solar salt (60 wt.%$NaNO_3$: 40 wt.%KNO_3 [25]) at a nanoparticle mass ratio of 1 wt.% [11, 26], which showed favorable specific heat capacity performance within the considered concentration range (Figure S1). The mixture was loaded into a planetary ball mill and ground at 200 rpm for 10 min to achieve a uniform dispersion of nanoparticles within the base salt. The molten salt nanofluid prepared with untreated SiO_2 nanoparticles was denoted as MSNF, while those prepared with V_O-engineered SiO_2 nanoparticles annealed for 5 h and 8 h were denoted as V_O-MSNF-5h and V_O-MSNF-8h, respectively. In addition, MD simulations were employed to characterize the thermophysical properties of V_O-MSNF, and the simulation system (model setup) is shown in Figure 1b.

The experimental values of c_p of solar salt, MSNF, V_O-MSNF-5h, and V_O-MSNF-8h are summarized in Figure 1c. The c_p of

16146840, 2026, 40, Downloaded from https://advanced.onlinelibrary.wiley.com/doi/10.1002/aenm.71588 by Bingyang Cao - Tsinghua University Library , Wiley Online Library on [28/10/2026]. See the Terms and Conditions (https://onlinelibrary.wiley.com/terms-and-conditions) on Wiley Online Library for rules of use; OA articles are governed by the applicable Creative Commons License

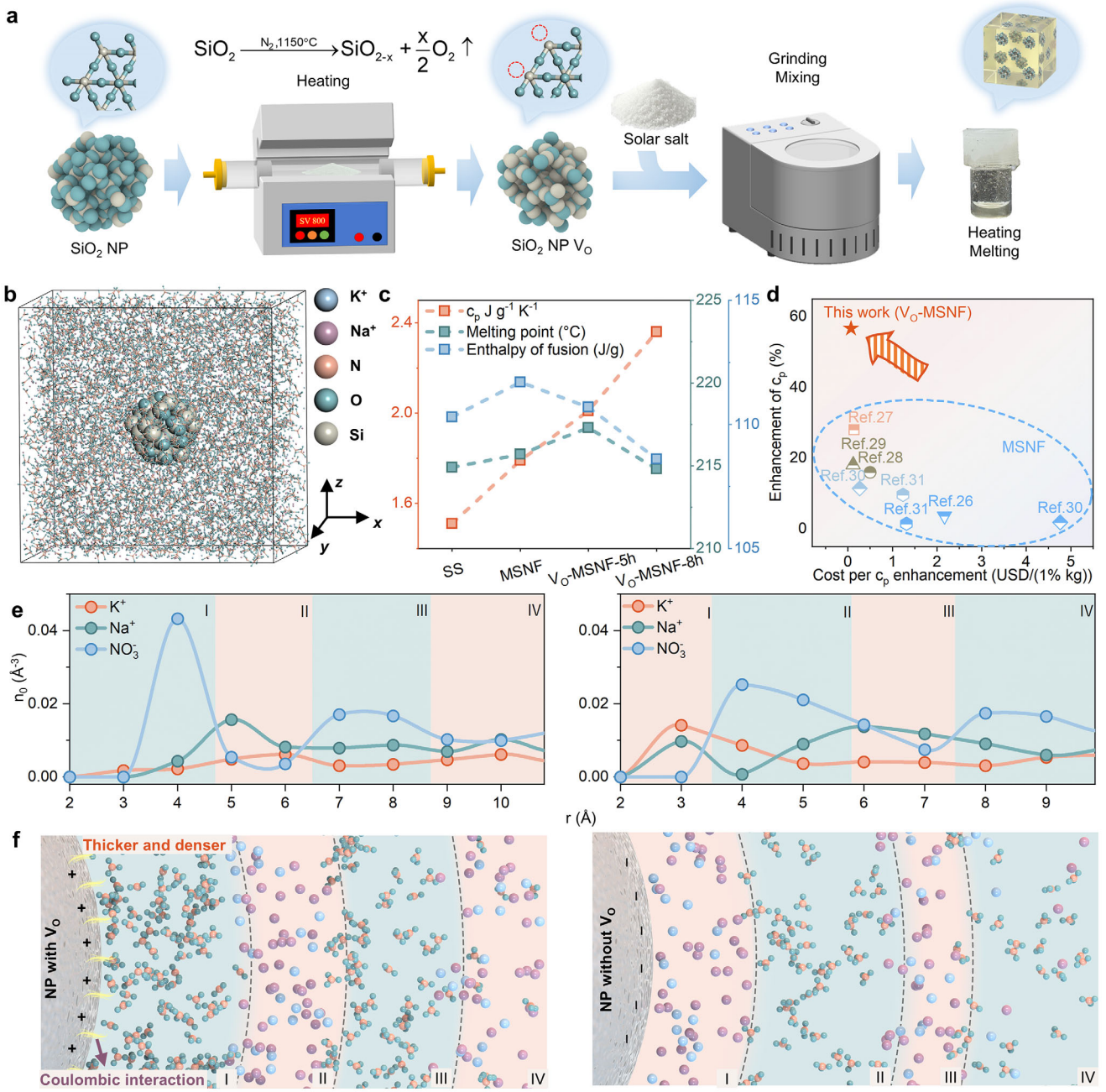


FIGURE 1 | Synthesis and heat capacity enhancement of V_O-MSNF. (a) Preparation process of V_O-MSNF. (b) MD simulation snapshots of MSNF system. (c) Specific heat capacity, melting point, and enthalpy of fusion of solar salt, MSNF, and V_O-MSNF. (d) Comparison of different MSNFs in terms of heat capacity enhancement and cost-effectiveness [26–31]. (e) Number density distributions at various density layers of V_O-MSNF (left) and MSNF (right) at 573 K. (f) Ion arrangement diagram of V_O-MSNF (left) and MSNF (right).

solar salt was initialized as a 1.51 ± 0.05 $J{\cdot}g^{-1}{\cdot}K^{-1}$ and increased to 1.79 ± 0.08 $J{\cdot}g^{-1}{\cdot}K^{-1}$ by introducing SiO_2 nanoparticles. Upon further introducing annealing-induced V_O, the value of c_p rose to 2.01 ± 0.10 and 2.36 ± 0.07 $J{\cdot}g^{-1}{\cdot}K^{-1}$ for V_O-MSNF-5h and V_O-MSNF-8h, corresponding to enhancements of 33.1% and 56.6%, respectively. The c_p improvement of V_O-MSNF-8h is more than three times that of MSNF, exceeding the previously reported c_p enhancement of 28% [27] by 28.6 percentage points, while maintaining a lower cost per 1% gain in c_p, as shown in Figure 1d.

Figure 1e,f presents the number density distributions of V_O-MSNF and MSNF systems at 573 K. Here, region I denotes the first interfacial ionic layer immediately adjacent to the nanoparticle surface. In MSNF, ion accumulation behavior was observed near the interface. Specifically, NO_3^- exhibited a peak at a distance of about 4 Å from the nanoparticle surface, while K^+ and Na^+ displayed smaller peaks at around 3 Å along with the peak intensity of K^+ being greater than that of Na^+. This indicates that the nanoparticles modulate the distribution of ions in the

16146840, 2026, 40, Downloaded from https://advanced.onlinelibrary.wiley.com/doi/10.1002/aenm.71588 by Bingyang Cao - Tsinghua University Library , Wiley Online Library on [28/10/2026]. See the Terms and Conditions (https://onlinelibrary.wiley.com/terms-and-conditions) on Wiley Online Library for rules of use; OA articles are governed by the applicable Creative Commons License

molten salt. In the system doped with SiO_2 nanoparticles with V_O, however, the ionic distribution exhibited a more distinct spatial layering structure. Such pronounced layering is a typical characteristic of an enhanced interfacial electric double layer (EDL) [32, 33]. The primary peak intensity of NO_3^- was increased by 71.4% and became more concentrated at the position of approximately 4 Å, suggesting stronger electrostatic adsorption of NO_3^- near the nanoparticle surface. The distinct K^+ peak near 3 Å almost disappeared, and its number density at this position was decreased by 87.5%. The Na^+ peak shifted from approximately 3–5 Å, while its peak intensity was increased by 61.3%, reflecting the redistribution of Na^+ away from the immediate vicinity of the nanoparticle surface. The corresponding quantitative peak parameters are summarized in Table S1. Overall, V_O induced a pronounced species-dependent redistribution of interfacial ions, characterized by enhanced NO_3^- accumulation, depletion of K^+ near the surface, and an outward shift of the preferred Na^+ accumulation region.

2.2 | Interfacial Ionic Structure and Mechanism of Heat Capacity Enhancement

Electron paramagnetic resonance (EPR) spectroscopy provided direct evidence of V_O formation within the SiO_2 lattice following the nitrogen annealing. While untreated SiO_2 nanoparticles showed negligible paramagnetic activity ($g \approx 2.00$), the sample annealed at 1150°C for 8 h exhibited a distinct symmetric derivative signal at 3510 G (g = 2.002-2.003), as shown in Figure 2a. This signature is characteristic of E′ centers, which correspond to the unpaired electrons on threefold-coordinated Si atoms associated with V_O [34]. It also confirms that the thermal treatment successfully introduced the specific point defects into the nanoparticle structure. X-ray photoelectron spectroscopy (XPS) measurements further showed that the Si 2p and O 1s peaks of V_O-SiO_2 shifted by approximately 0.33 and 0.30 eV, respectively, toward lower binding energy compared to SiO_2 (Figure S2). Similar lower-binding-energy shifts have been reported for oxygen-deficient silica [35], supporting a defect-induced modification of the surface electronic environment of SiO_2. Density functional theory (DFT) was used to optimize the charge distribution characteristics of SiO_2 nanoparticles with V_O defects compared to those without defects, as shown in Figure 2b. To characterize the charge distribution of the optimized SiO_2 nanoparticles, they were divided into five concentric spherical shells with equivalent thickness and the innermost layer being the ball. These five shells were numbered by an order from the inside, and the atomic charges within each shell were summed to determine the overall charge distribution. The net charges of the different shells in ordinary SiO_2 nanoparticles are all close to zero, indicating a relatively uniform charge distribution without obvious charge segregation, while the nanoparticles with V_O exhibit significant positive charge accumulation on the surface.

The charge density distribution in Figure 2c further revealed the differences of interfacial charge structures among the MSNF and V_O-MSNF systems. To quantitatively determine the outer boundary of the first interfacial ionic layer (e.g., region I), we defined it as the first zero-crossing zone of the local charge-density profile following the first pronounced interfacial charge-density extremum. According to this criterion, the outer boundary was located at approximately 3.6 Å for MSNF and 4.7 Å for V_O-MSNF, indicating an outward extension of approximately 1.1 Å after the introduction of V_O. In the MSNF system, the profile of radial charge density shows clear oscillations near the nanoparticle surface. These oscillations, which arise from the alternating accumulation of positive and negative charges, indicate that the interfacial ions are rearranged to form a layered charge structure. In the V_O-MSNF system, the charge oscillations became more pronounced and exhibited higher peak intensities and more concentrated distributions, resulting in a clearer alternation of positive and negative charge layers and the formation of a typical charge layering structure. The charge density in MSNF had been decreased to 0.00146 at 10 Å from the nanoparticle surface, approaching the near-zero far-field fluctuation level. In contrast, V_O-MSNF retained a pronounced value of 0.00643 at the same distance, approximately 4.4 times higher than that of MSNF, and its charge-density oscillation gradually decayed toward the near-zero level at approximately 13 Å. As the temperature increased, the amplitude of charge density fluctuations decreased slightly (Figure S3). However, the SiO_2 nanoparticles with V_O-engineered system retained strong layering characteristics, indicating that its interfacial structure possesses enhanced stability under high-temperature conditions.

The experimental values of c_p for solar salt, MSNF, V_O-MSNF-5h, and V_O-MSNF-8h over the temperature range of 573–773 K are shown in Figure 2d. Their average values of c_p are 1.51 ± 0.05, 1.79 ± 0.08, 2.01 ± 0.10 and 2.36 ± 0.07 $J{\cdot}g^{-1}{\cdot}K^{-1}$, respectively. Overall, the experimental c_p values of all samples gradually increase with increasing temperature, which is consistent with the trends reported other reports [26, 36]. MD simulations were used to calculate c_p of the solar salt, MSNF, and V_O-MSNF systems at a temperature range of 573–773 K, as shown in Figure 2d. The calculated average c_p of solar salt is 1.47 $J{\cdot}g^{-1}{\cdot}K^{-1}$, which deviates less than 2% compared to the literature values [37], validating the simulation results. Incorporating untreated SiO_2 nanoparticles yields an average c_p of 1.570 $J{\cdot}g^{-1}{\cdot}K^{-1}$, corresponding to an increase of 6.8% over the solar salt, whereas V_O-engineered SiO_2 produces the most pronounced enhancement, i.e., c_p of 1.84 $J{\cdot}g^{-1}{\cdot}K^{-1}$, corresponding to a 25.2% increase. Notably, the experimentally measured specific heat capacity increased with temperature, whereas the MD-calculated value decreased. Similar differences have been reported previously: positive temperature dependences were observed experimentally for SiO_2-containing nitrate nanofluids [36, 38], while decreasing trends were obtained from MD simulations [16]. This discrepancy reflects the limited ability of current classical force fields to reproduce the temperature dependence of heat capacity in molten-salt systems. Similar decreasing trends have also been observed in MD simulations of pure and mixed molten salts, where the decrease in heat capacity was interpreted in terms of the reduction of transverse collective modes at elevated temperatures [39]. Overall, the discrepancy highlights that the current classical MD model does not fully reproduce the temperature-dependent heat-capacity behavior of real molten-salt systems, although it remains useful for comparing relative differences among the simulated systems and examining their microscopic origins. In addition, the simulations underestimate the magnitude of the c_p enhancement relative to the experimental values. This quantitative discrepancy is mainly attributed to the necessary simplifications in the MD model, particularly the smaller nanoparticle size and the

16146840, 2026, 40, Downloaded from https://advanced.onlinelibrary.wiley.com/doi/10.1002/aenm.71588 by Binglyang Cao - Tsinghua University Library , Wiley Online Library on [28/10/2026]. See the Terms and Conditions (https://onlinelibrary.wiley.com/terms-and-conditions) on Wiley Online Library for rules of use; OA articles are governed by the applicable Creative Commons License

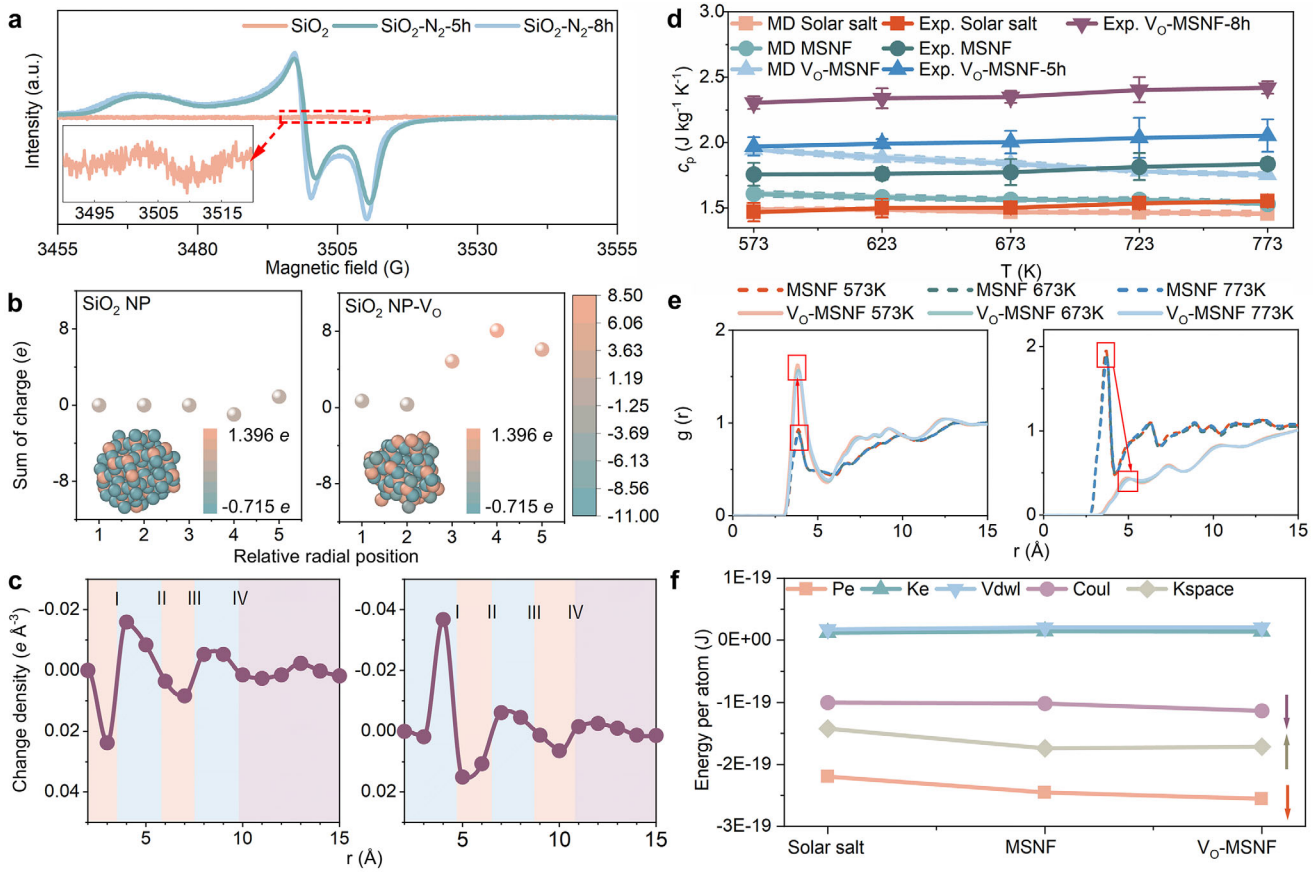


FIGURE 2 | Interfacial mechanism of heat capacity enhancement in V_O-MSNF (a) EPR spectra of SiO_2 nanoparticles. (b) Charge distribution of SiO_2 nanoparticles. (c) Charge density distributions of MSNF (left) and V_O-MSNF (right) at 573 K. (d) Specific heat capacity of solar salt, MSNF, and V_O-MSNF at different temperatures. (e) RDF curves of Si-N and Si-K^+. (f) Energy of solar salt, MSNF, and V_O-MSNF per atom at 573K in MD simulations.

idealized interfacial structure, which may weaken the role of interfacial ion structuring in real systems and thus lead to an underestimation of the c_p enhancement [36, 40–42]. Overall, although some quantitative deviations from the experimental results remain, the simulations consistently capture the relative trends among different systems.

Figure 2e presents the RDF curves of Si with Na^+, K^+, and NO_3^- ions in both MSNF and V_O-MSNF. The introduction of V_O defects shifted the main Si-Na^+ RDF peak slightly toward a larger radial distance, accompanied by a pronounced increase in peak intensity, as shown in Figure S4. This indicates that V_O enhanced the interfacial repulsion of Na^+, causing Na^+ ions to move farther away from the nanoparticle surface. The corresponding cumulative coordination-number profiles are presented in Figure S5, and the calculated coordination numbers and cutoff distances are summarized in Table S2. The Si-Na coordination numbers increased from 0.310, 0.289, and 0.276 in MSNF to 1.636, 1.579, and 1.425 in V_O-MSNF at 573, 673 and 773 K, respectively, while the corresponding cutoff distance increased from approximately 4.09–5.51–5.59 Å, indicating that Na^+ ions were redistributed away from the nanoparticle surface and accumulated more densely in an outer interfacial region. For the Si-K^+ RDF curve, the MSNF system exhibited a distinct main peak, while the peak almost vanished in V_O-MSNF system, suggesting that the presence of K^+ near the V_O-engineered SiO_2 was significantly suppressed. This trend is consistent with the number density results discussed earlier. For the Si-N curve, the introduction of V_O defects leads to a significant enhancement of the main peak, indicating a denser accumulation of NO_3^- ions near the nanoparticle surface. The Si-N coordination numbers increased from 1.358, 1.288, and 1.225 in MSNF to 3.484, 3.406, and 3.297 in V_O-MSNF at 573, 673, and 773 K, respectively, confirming the enhanced interfacial enrichment of NO_3^-. Increasing temperature reduced the intensity of all RDF peaks and shifted the peak positions outward, reflecting weakened local structural correlations between the nanoparticles and ions with increased ionic kinetic activity. Nevertheless, the adsorption of anions onto the V_O-engineered nanoparticles remained relatively stable.

Figure 2f shows the decomposition of the total energy into different components for solar salt, MSNF, and V_O-MSNF at 573 K from MD simulations. Overall, introducing nanoparticles lowers the system potential energy, indicating strengthened interactions between the molten salt and nanoparticles, and the further reduced potential energy of V_O-MSNF after introducing V_O. This potential energy decrease is dominated by the electrostatic contributions: upon nanoparticle addition, the Coulombic term becomes more negative, indicating stronger electrostatic attraction, and it decreases further in V_O-MSNF, implying stronger overall electrostatic interactions in the system. In contrast, the kinetic energy only slightly changes, suggesting that the enhancement of c_p is not due to the increased ionic kinetic activity but rather arising from the strengthened particle-ion interactions and

16146840, 2026, 40, Downloaded from https://advanced.onlinelibrary.wiley.com/doi/10.1002/aenm.71588 by Bingyang Cao - Tsinghua University Library , Wiley Online Library on [28/10/2026]. See the Terms and Conditions (https://onlinelibrary.wiley.com/terms-and-conditions) on Wiley Online Library for rules of use; OA articles are governed by the applicable Creative Commons License

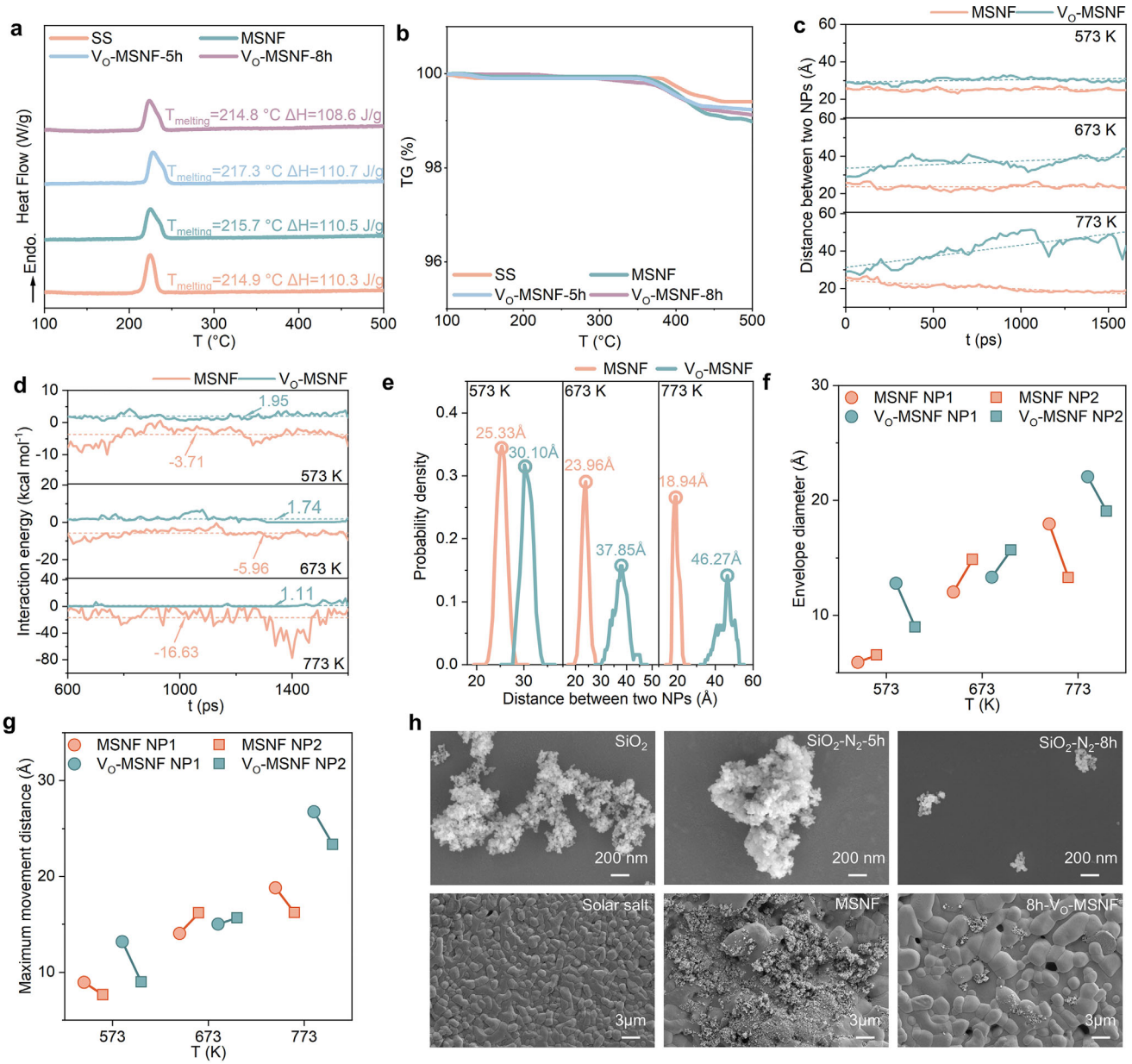


FIGURE 3 | Thermal and dispersion stability of V_O-MSNF. (a,b) DSC and TG curves of solar salt, MSNF, and V_O-MSNF. (c,d) Geometric center distance and interaction energy between nanoparticles in MSNF and V_O-MSNF. (e) Probability distributions of nanoparticles distance of MSNF and V_O-MSNF in MD simulations. (f,g) Envelope diameter and maximum movement distance of nanoparticles in MSNF and V_O-MSNF in MD simulations. (h) SEM images of nanoparticles at 50,000× magnification (top) and MSNF (bottom) at 3,000× magnification.

a deeper potential-energy well, which therefore demands a larger energy uptake per unit temperature rise.

2.3 | Thermal Stability and Dispersion Stability of V_O-MSNF

To evaluate the thermal stability of V_O-MSNF, differential scanning calorimetry (DSC) and thermogravimetry analysis (TG) tests were performed on the four systems, as shown in Figure 3a,b. Upon the introduction of V_O-engineered SiO_2 nanoparticles, the phase transition thermodynamics of the molten salt remained robust, characterized by a stable melting point within the temperature range of 214°C–218°C and an enthalpy of fusion fluctuating marginally between 108 and 112 J/g. TG results show negligible mass loss below 350°C and only a slight decrease above 370°C; all samples retain >98.9% mass at 500°C, indicating that V_O-engineered SiO_2 does not noticeably reduce the thermal stability.

A dual-particle model was constructed for the MSNF and V_O-MSNF systems to evaluate the influence of V_O defects on nanoparticle dispersion in molten salt, as shown in Figure S6. The variations in interparticle geometric distance and interaction energy were tracked during the long-term evolution in a high-temperature environment at an initial surface-to-surface distance set to 12 Å. For each system, the total simulation duration was 1.6 ns, and the final 1.0 ns was used as the production simulation.

16146840, 2026, 40, Downloaded from https://advanced.onlinelibrary.wiley.com/doi/10.1002/aenm.71588 by Bingyang Cao - Tsinghua University Library , Wiley Online Library on [28/10/2026]. See the Terms and Conditions (https://onlinelibrary.wiley.com/terms-and-conditions) on Wiley Online Library for rules of use; OA articles are governed by the applicable Creative Commons License

Figure 3c shows the trajectories of the geometric center-to-center distance and interaction energy of the particles in the temperature range of 573–773 K. At 573 K, the interparticle distances in both systems remained close to the initial value, with only slight fluctuations due to the thermal perturbations and no apparent attraction- or repulsion-dominated motion. At 673 K, the MSNF system showed a marginal tendency toward aggregation, whereas the interparticle distance gradually increased in the V_O-MSNF system, indicating that the introduction of V_O enhanced the repulsive interactions between nanoparticles, which made them slowly departure during the statistically observed period. At the elevated temperature of 773 K, the nanoparticles in the MSNF system approached each other significantly over time, with the minimum center-to-center distance decreasing to approximately 17.62 Å, indicating a pronounced pairwise agglomeration tendency. In contrast, the interparticle distance in the V_O-MSNF system gradually increased with time without any aggregation tendency, reflecting that the V_O-engineered nanoparticles maintained good dispersion stability even at high temperatures. During the final 1.0 ns production period, the average center-to-center distances in MSNF were 25.20, 23.65, and 19.29 Å at 573, 673, and 773 K, respectively, whereas the corresponding values in V_O-MSNF were 30.70, 37.59, and 45.23 Å. The corresponding interaction energies in Figure 3d further confirmed the above behaviors of movement. For MSNF, the interparticle interaction energies were negative at all three temperatures, and the lowest value was observed at 773 K, indicating the enhanced attraction between particles. In contrast, the interaction energies of V_O-MSNF remained close to zero and slightly increased at 673 and 773 K, suggesting a repulsive tendency. These results indicate that V_O defects effectively regulate the interaction potential between nanoparticles, thereby increasing effective interparticle repulsion and helping maintain nanoparticle dispersion, particularly at elevated temperatures.

Furthermore, Figure 3e presents the probability distributions of the interparticle distances extracted from the trajectories in Figure 3c. For MSNF, the most probable distance shifts from 25.33 Å at 573 K to 23.96 Å at 673 K and further to 18.94 Å at 773 K, confirming that the defect-free particles tend to move closer and eventually aggregate as temperature rises. In contrast, the distance distribution of V_O-MSNF shifts monotonically toward larger separations, with peak positions at 30.10, 37.85, and 46.27 Å for 573, 673, and 773 K, respectively, demonstrating that V_O defects promote and stabilize larger interparticle separations and thus favor the long-term dispersion of nanoparticles in the molten salt.

Figure 3f,g presents the statistical results of the envelope diameter and the maximum displacement of the particle center's motion trajectory at different temperatures. The maximum displacement refers to the farthest distance reached by a nanoparticle from its initial position, reflecting its largest spatial excursion under thermal driving, whereas the trajectory envelope diameter characterizes the maximum spatial range covered during the entire simulation process. The V_O-MSNF system exhibited larger motion ranges than the MSNF system at all temperatures, indicating broader spatial exploration. At 573 K, the motion ranges of the nanoparticles in both systems were similar and only had minor differences. When the temperature increased to 673 K, the motion range of V_O-MSNF expanded significantly, with both the envelope diameter and the maximum displacement exceeding those of MSNF. At 773 K, the differences became more pronounced, with the maximum displacements of the two nanoparticles in V_O-MSNF reaching 26.772 and 23.317 Å, respectively, which were substantially greater than those of 18.813 and 16.203 Å observed in MSNF. Connecting with the interparticle-distance analysis, these results suggest that V_O defects enhance the dispersion stability of nanoparticles in molten salt while providing greater freedom of motion at elevated temperatures.

The SEM images in Figures 3h (top) and S7a–f depict the dispersion states of SiO_2, SiO_2-N_2-5h, and SiO_2-N_2-8h after being dispersed in ethanol at the same concentration and ultrasonicated for 15 min. Untreated SiO_2 forms loose, large clusters, whereas SiO_2-N_2-5h shows smaller aggregates. SiO_2-N_2-8h exhibits more refined and uniformly distributed nanoparticle clusters. These results indicate that prolonging N_2 treatment duration effectively improves SiO_2 dispersibility by regulating the aggregation behavior. The SEM images in Figures 3h (bottom) and S7g–l illustrate the dispersion states of nanoparticles in molten salts. In MSNF system, nanoparticles tend to adhere to the salt surface and form moderate clusters. In contrast, V_O-MSNF-8h presents a finer dispersion pattern with particles more homogeneously embedded in the matrix. Overall, V_O-MSNF-8h demonstrates a tendency toward improved nanoparticle dispersion compared to MSNF, supporting the crucial role of V_O in enhancing the stability of molten salt nanofluids.

Thermal cycling tests were further conducted in an air environment to assess the durability of the enhanced specific heat capacity. After five cycles, the average specific heat capacity of V_O-MSNF was 2.24 J g^{-1} K^{-1}, corresponding to approximately 94.8% of its initial value. Only limited variation was observed with continued cycling, and the specific heat capacity remained at a comparable level from 15 to 30 cycles. The specific heat capacity retention was 93.2% and 93.7% after 15 and 30 cycles, respectively (Figure S8), with the degradation remaining within the ~8% range reported for other molten-salt nanofluids [43, 44]. Overall, V_O-MSNF retained most of its enhanced specific heat capacity after repeated heating and cooling. The post-cycling morphology of V_O-MSNF was further examined by SEM. As shown in Figure S9, the nanoparticles in V_O-MSNF fairly remained uniform distribution after 30 thermal cycles, with no obvious agglomeration observed, demonstrating good morphological stability during thermal cycling.

2.4 | Thermal Conductivity and Viscosity of V_O-MSNF

The thermal conductivities of three systems were experimentally measured in the liquid-state temperature regime, and the experimental values are summarized in Figure 4a. The measured thermal conductivities were 0.491 W/m·K, 0.656 W/m·K, and 0.789 W/m·K for the solar salt, MSNF, and V_O-MSNF, respectively. Taking solar salt as the baseline, the experimental enhancement strength of MSNF and V_O-MSNF reached 33.62% and 60.81%. The experimental thermal conductivity of solar salt is consistent with the reported value of 0.5 W/m·K in the literature [45].

16146840, 2026, 40, Downloaded from https://advanced.onlinelibrary.wiley.com/doi/10.1002/aenm.71588 by Bingyang Cao - Tsinghua University Library , Wiley Online Library on [28/10/2026]. See the Terms and Conditions (https://onlinelibrary.wiley.com/terms-and-conditions) on Wiley Online Library for rules of use; OA articles are governed by the applicable Creative Commons License

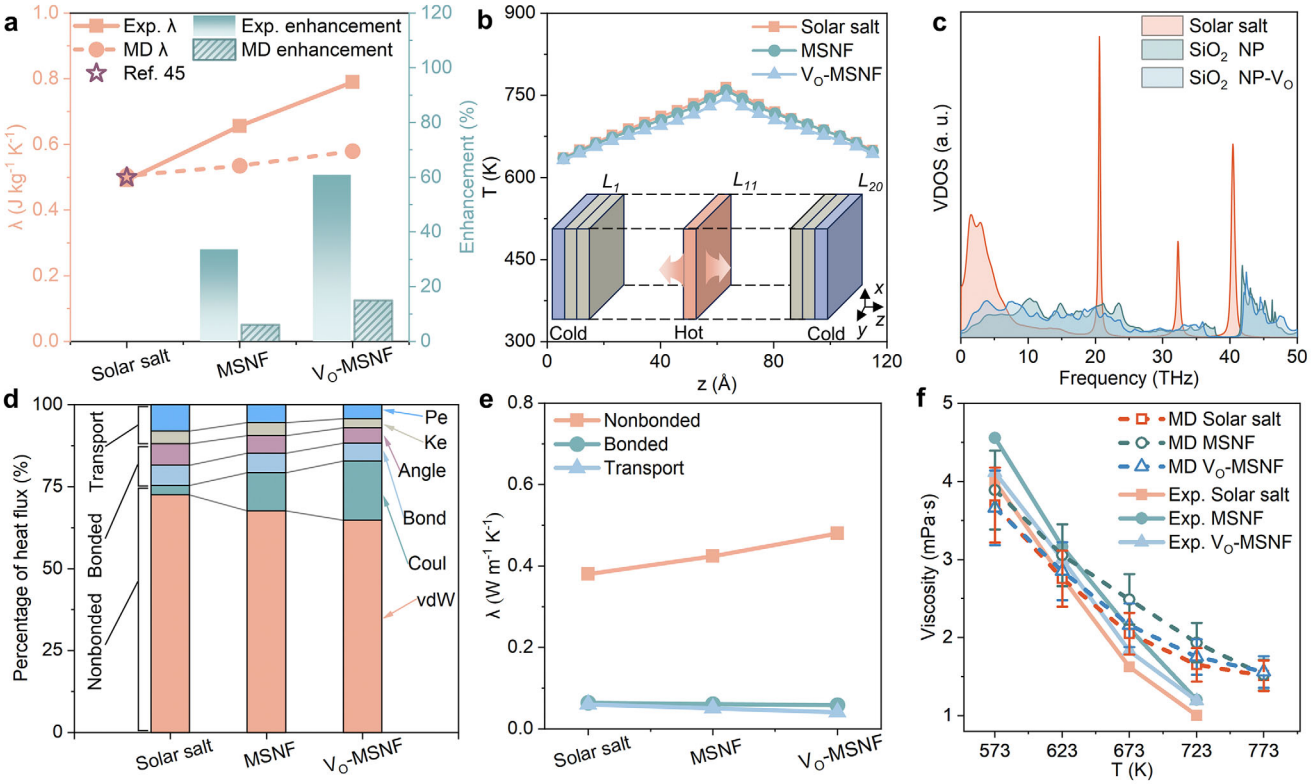


FIGURE 4 | Thermal transport and viscosity of V_O-MSNF. (a) Thermal conductivity of solar salt, MSNF and V_O-MSNF-8h. (b) Temperature profiles of solar salt, MSNF and V_O-MSNF. (c) VDOS curves of solar salt, SiO_2 NP, and SiO_2 NP-V_O. (d,e) Heat flux decomposition of solar salt, MSNF and V_O-MSNF: d, Proportion of heat flux and e, partial thermal conductivity. (f) Viscosity of solar salt, MSNF, and V_O-MSNF-8h at different temperatures.

The thermal conductivity was then calculated using the Reverse Non-Equilibrium Molecular Dynamics (RNEMD) method within the temperature range of 630–770 K. To ensure a linear temperature response and sufficient sampling of the heat flux, the simulation box was extended in the heat flow direction with an aspect ratio of $x{:}z$ = 1:2.5. Figure 4a,b presents the temperature distribution and the thermal conductivity variation of solar salt, MSNF and V_O-MSNF systems. As shown in Figure 4b, a distinct linear temperature gradient was established between the heat source and heat sink across all systems, demonstrating stable heat flux channels and a reliable steady-state transfer process. The introduction of nanoparticles slightly affected the temperature distribution profiles but did not significantly disrupt the continuity or symmetry of the thermal field. As shown in Figure 4a, the simulated thermal conductivities of solar salt, MSNF, and V_O-MSNF were 0.504 W/m·K, 0.534 W/m·K, and 0.579 W/m·K, respectively, indicating more pronounced thermal conductivity enhancement with the introduction of V_O.

From a vibrational perspective, the VDOS spectra presented in Figure 4c provide further insight into the enhancement mechanism. As shown in Figure 4c, the VDOS of solar salt is mainly distributed near 0–10, 20, and 40 THz. The spectrum of SiO_2 nanoparticles partially overlaps with that of the solar salt in the mid-to-low frequency region, exhibiting a certain degree of vibrational frequency matching. With the introduction of V_O defects, however, the nanoparticles exhibited more pronounced vibrational enhancements in the low-frequency domain 5–15 THz, with an expanded frequency coverage and stronger intensities, particularly in the overlapping frequency range with the solar salt. Low-frequency vibration, due to their long mean free paths and lower scattering probabilities, play a key role in thermal transport [46]. Therefore, the introduction of V_O defects enhances the vibrational coherence between nanoparticles and the molten salt in the low-frequency region, thereby improving the interfacial vibrational matching and coupling efficiency, which in turn promotes the overall heat transfer performance of the system. In addition, the overlap of the VDOS between nanoparticle-doped systems and the solar salt was calculated. The overlap value for the MSNF was 0.3613, while that for the V_O-MSNF increased to 0.4599. The increase in overlap indicates that the introduction of V_O defects enhanced the vibrational mode compatibility between nanoparticles and the molten salt, which helps reduce the interfacial thermal resistance and thereby improve the overall thermal conductivity of the system.

To investigate how nanoparticles with V_O affect the thermal conductivity of molten salt, we monitored the microscopic composition of the molten salt macroscopic heat flow in simulations. Figure 4d,e presents the contributions of various energy terms to the heat flux and thermal conductivity in different systems. In this analysis, the heat flux components were decomposed into six types of interactions: vdW (van der Waals), Coul (electrostatic), Bond (bond stretching), Angle (angle bending), Ke (kinetic energy), and Pe (potential energy). Although the dihedral and improper dihedral terms exist in nanoparticles, their proportions in the system are negligible and thus were not included in the heat flux decomposition [47].

16146840, 2026, 40, Downloaded from https://advanced.onlinelibrary.wiley.com/doi/10.1002/aenm.71588 by Bingyang Cao - Tsinghua University Library , Wiley Online Library on [28/10/2026]. See the Terms and Conditions (https://onlinelibrary.wiley.com/terms-and-conditions) on Wiley Online Library for rules of use; OA articles are governed by the applicable Creative Commons License

In all three systems, the non-bonded interaction terms consistently dominated the heat flux pathways, accounting for 75% to 83% of the total thermal conductivity, and exhibited a gradual increase with nanoparticles doping and defect introduction. A further breakdown revealed that this enhancement was primarily driven by the Coulombic interaction term, indicating that the charge redistribution induced by doping significantly strengthened the electrostatic interactions between ions, to further thereby enhance the nonbonded contribution to heat transport. The bonded interactions remained at approximately 5%–7% for bond terms and about 4%–7% for angle terms, respectively. Their limited and slightly decreasing contributions across the series indicate that bonded interactions only play a secondary role in the entire thermal transport mechanism. The contribution from transport terms decreased from about 12% in solar salt to 7% in V_O-MSNF, demonstrating that as the interfacial coupling was enhanced, the contribution associated with microscopic transport and local atomic motions gradually decreased.

Figure 4e quantitatively illustrates the contributions of each component to the thermal conductivity, further confirming the above trends. The contribution of non-bonded terms to the thermal conductivity increased from approximately 0.38 $W{\cdot}m^{-1}{\cdot}K^{-1}$ in solar salt to 0.48 $W{\cdot}m^{-1}{\cdot}K^{-1}$ in V_O-MSNF, representing the largest enhancement among all interactions. The bonded terms remained stable within the range of 0.05–0.07 $W{\cdot}m^{-1}{\cdot}K^{-1}$ and showed no significant variation with doping, indicating that changes in bonded structures were not the dominant factor affecting the thermal conductivity. In contrast, the contribution of transport terms decreased from about 0.06 $W{\cdot}m^{-1}{\cdot}K^{-1}$ in solar salt to 0.04 $W{\cdot}m^{-1}{\cdot}K^{-1}$ in V_O-MSNF.

Taken together, these results indicate that the enhanced thermal conductivity of V_O-MSNF should be understood as arising from coupled contributions rather than from a single mechanism. The atomistic results identify strengthened non-bonded electrostatic interactions and enhanced interfacial vibrational coupling as important microscopic contributions, while the improved nanoparticle dispersion observed experimentally may also facilitate the heat transport.

Finally, Figure 4f shows the temperature-dependent viscosities of solar salt, MSNF, and V_O-MSNF from experiments and MD simulations. For all systems, the viscosity decreases markedly with increasing temperature. In the experimental results, both nanofluids exhibit higher viscosities than solar salt, while V_O-MSNF shows a slightly lower viscosity than MSNF. The MD simulations reproduce the same overall tendency, confirming that nanoparticle addition increases viscous resistance, whereas V_O modification partially mitigates this effect. In addition, the viscosity differences among the three systems gradually diminish at higher temperatures. The above viscosity evolution is consistent with the self-diffusion results as shown in Figure S10. The self-diffusion coefficients of solar salt, MSNF, and V_O-MSNF increased from 9.36×10^{-10}, 8.87×10^{-10}, and 9.14×10^{-10} m^2/s at 573 K to 3.05×10^{-9}, 2.99×10^{-9}, and 3.03×10^{-9} m^2/s at 773 K, respectively, indicating enhanced ion mobility and reduced resistance to flow with the increasing of temperature. At the same temperature, MSNF consistently exhibited the lowest self-diffusion coefficient, whereas the values of V_O-MSNF were 3.1%, 5.5% and 1.3%, which are higher than those of MSNF at 573, 673 and 773 K, respectively, and remained closer to those of solar salt. This inverse correlation between the self-diffusion and viscosity indicates that nanoparticles hinder ion migration and increase microscopic internal friction, whereas V_O modification partially alleviates this transport limitation by altering the interfacial environment between the nanoparticles and molten-salt ions.

2.5 | Techno-Economic Analysis of V_O-MSNF in TES

As molten-salt-based materials continue to advance for high-temperature solar thermal storage, the material-level thermophysical improvement needs to be evaluated at the system level [48]. At the TES component level, the primary techno-economic advantage of V_O-MSNF is that its enhanced c_p reduces the required amount of TES medium and downsizing the storage device. Compared with the baseline solar salt case, the use of V_O-MSNF reduces the mass of TES medium by 34.22%. The reduced material requirement lowers the TES medium cost by 29.17%. The less TES medium also decreases the TES volume by 34.30%, resulting in a 28.30% reduction in the storage device cost. The detailed values and cost are provided in Table S3. Collectively, the simultaneous reductions in TES medium cost and storage device cost establish V_O-MSNF as a cost-effective TES option by converting thermophysical-property enhancement into tangible capital savings. It should be noted that the present cost analysis includes the raw-material cost of SiO_2 nanoparticles but does not explicitly account for the additional processing cost associated with V_O creation, which requires further evaluation for large-scale production.

The plant-level CSP performance can benefit from the enhanced TES. The schematic diagram of the involved system, as well as the parameters of the weather and heliostat field, are shown in Figures 5a,b and S11. Figure 5c–f compare the LCOE and AEG of the solar salt, MSNF, and V_O-MSNF in parabolic trough collector-Rankine cycle, solar power tower-Brayton cycle, and solar power tower-Rankine cycle (PTC-RC, SPT-BC, and SPT-RC), calculated using System Advisor Model (SAM) [49] under the identical weather and operating conditions. Two design strategies are considered: FC (fixed thermal capacity of TES) and FV (fixed storage volume of TES). Figure 5c,d present the absolute values of LCOE and AEG, while Figure 5e,f shows the performance improvement of V_O-MSNF compared to the solar salt.

Under FC condition, the enhancement effect of V_O-MSNF on c_p primarily reduces the TES medium and storage volume, resulting in a reduction of 3.89% in LCOE for the PTC-RC system. Under FV condition, the impact of V_O-MSNF on different systems shows obviously different characteristics. The LCOE improvement rate reaches 4.22%–4.56%, and the AEG increase exceeds 6.40% in the SPT system, respectively. In contrast, the PTC-RC system shows intensive response under the same FV conditions. Its LCOE has only improved by 0.52%, and the increase in AEG is significantly lower than that of the tower system. The greater benefit of V_O-MSNF in the SPT systems is mainly attributed to the more effective utilization of the increased TES capacity and the higher cycle thermal efficiency. Under the FV condition, the annual TES discharge was increased by 11.49% in the SPT system after replacing the solar salt with V_O-MSNF, compared with only

16146840, 2026, 40, Downloaded from https://advanced.onlinelibrary.wiley.com/doi/10.1002/aenm.71588 by Bingyang Cao - Tsinghua University Library , Wiley Online Library on [28/10/2026]. See the Terms and Conditions (https://onlinelibrary.wiley.com/terms-and-conditions) on Wiley Online Library for rules of use; OA articles are governed by the applicable Creative Commons License

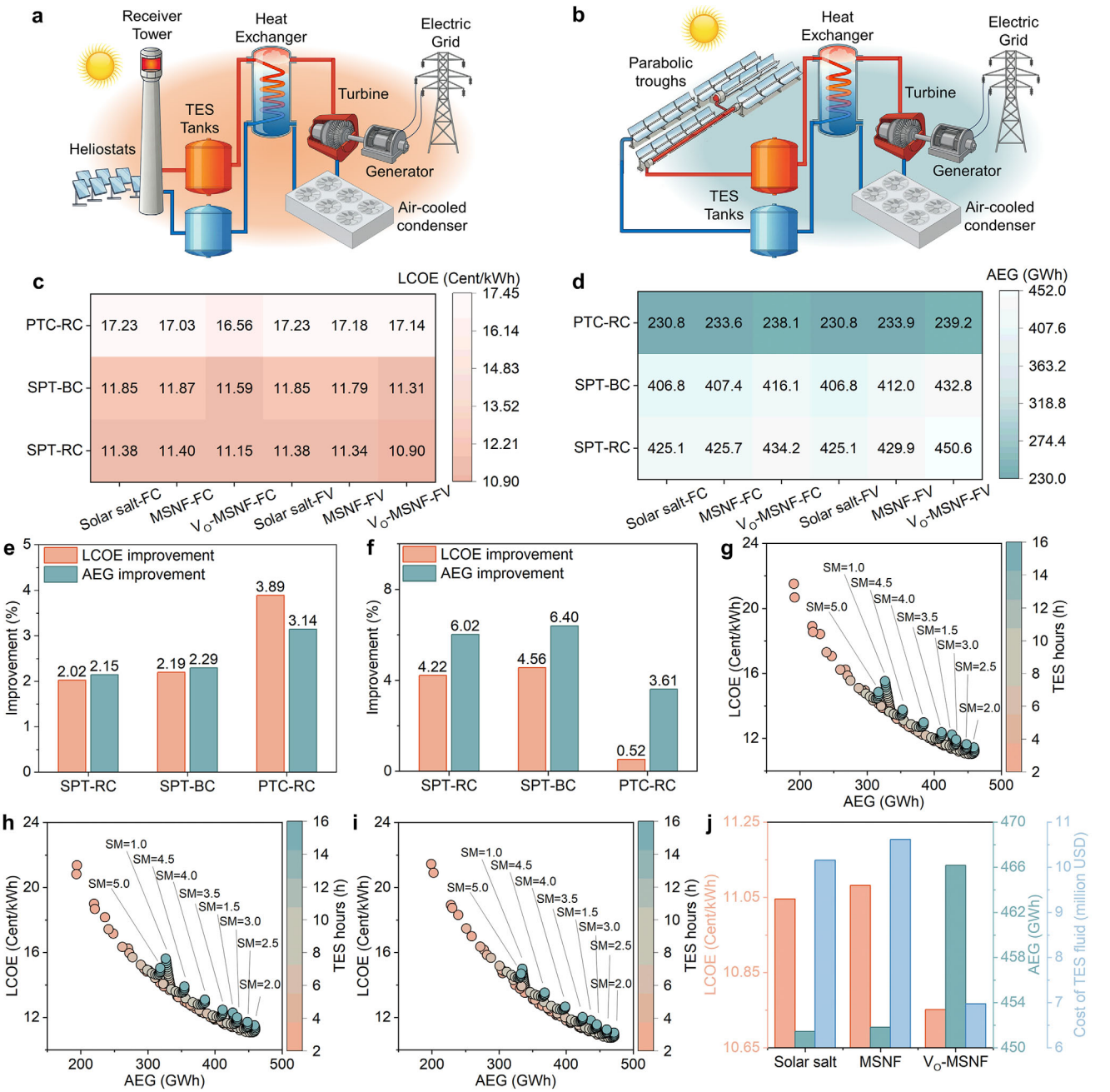


FIGURE 5 | System-level performance of CSP systems employing V_O-MSNF. (a,b) Diagram of the solar power tower system and parabolic trough plant. (c,d) LCOE and AEG of the solar salt, MSNF and V_O-MSNF under three power cycles (PTC-RC, SPT-BC, and SPT-RC), FC and FV. (e,f) Corresponding changes in LCOE and AEG of V_O-MSNF compared to solar salts under the FC and FV conditions. (g–i) Parametric analysis results showing the variation in LCOE and AEG for the SPT-RC system with varying SM and TES hours. The scatter plots represent the system performance using g, solar salt, h, MSNF, and i, V_O-MSNF as the thermal energy storage medium. (j) Comparison of the LCOE, AEG, and TES fluid cost for the three TES fluids under the selected SM and TES hours combinations.

1.61% in the PTC-RC system, as illustrated in Table S4. Together with the higher cycle thermal efficiency of the SPT systems, this greater TES utilization results in a larger improvement in AEG and consequently a more pronounced reduction in LCOE.

To further explore the maximum potential of the nanofluids, a parametric analysis of Solar Multiple (SM) and TES hours was conducted for the SPT-RC system, as illustrated in Figure 5g–i. SM was varied from 1 to 5 at an interval of 0.5, while TES hours were varied from 2 to 16 h at an interval of 1 h. A SAM simulation was performed for each parameter combination to obtain the corresponding LCOE and AEG. Based on the combined consideration of minimizing LCOE and maximizing AEG, the selected configurations were SM = 2 and TES hours = 9 h for both solar salt and MSNF, and SM = 2 and TES hours = 10 h for V_O-MSNF. The corresponding results were extracted and compared in Figure 5j. For MSNF, although the enhanced thermal properties contribute to a marginal increase in AEG

16146840, 2026, 40, Downloaded from https://advanced.onlinelibrary.wiley.com/doi/10.1002/aenm.71588 by Bingyang Cao - Tsinghua University Library , Wiley Online Library on [28/10/2026]. See the Terms and Conditions (https://onlinelibrary.wiley.com/terms-and-conditions) on Wiley Online Library for rules of use; OA articles are governed by the applicable Creative Commons License

to 451.83 GWh, this gain is accompanied by a rise in LCOE to 11.08 Cents/kWh. This economic penalty is primarily attributed to the higher TES medium cost of $10.61m, which outweighs the benefits of enhanced thermal properties. In contrast, V_O-MSNF demonstrates a superior outcome by achieving the highest AEG of 466.15 GWh and the lowest LCOE of 10.75 Cents/kWh. This economic efficiency is fundamentally driven by the drastic reduction in the costs of TES medium and storage device.

3 | Conclusion

Experiments combined with MD simulations of V_O-MSNF showed key findings: 1 wt.% doping enhanced c_p by up to 56.6%, which tripled the enhancement effect of thermal energy storage of the nanoparticle-reinforced solar salt without V_O. An increase of 60% in the thermal conductivity was also observed, alongside a stable melting point and enthalpy. Mechanistically, the V_O-engineered nanoparticles function as localized charge centers that drive the strong electrostatic adsorption of NO_3^-, leading to denser and thicker ionic compression layers. The introduction of V_O intensifies the interaction between the nanoparticles and the molten salt, enhancing the heat storage capacity of the molten salt. Furthermore, these defects amplify the low-frequency vibrational coupling between the nanoparticles and the molten salt and optimize the VDOS overlap that effectively reduces the interfacial thermal resistance. The V_O defects also govern the fluid stability by generating repulsive interparticle potentials, which can effectively suppress the high-temperature agglomeration and mitigate the substantial viscosity increase. Techno-economic analysis shows that the use of V_O-MSNF lowers the LCOE and increases the annual power generation, particularly in solar power tower configurations. Consequently, V_O-engineered nanofluids provide a promising option for improving the efficiency and economic viability of CSP systems using solar salts as the thermal storage medium.

Several limitations of the present work should be acknowledged. The experimental validation is currently limited to the SiO_2/solar salt system. It should be noted that the proposed defect-engineering method may be applicable to a broad range of molten-salt nanofluids, but its broader applicability requires further validation using other molten salts and nanoparticles. The dual-particle model was employed to isolate the fundamental influence of V_O defects on interparticle interactions. Future simulations involving multiple nanoparticles are required to capture the collective aggregation behavior. Although SEM observations support the improved dispersion after solidification, future in situ characterization at elevated temperatures is required to validate the nanoparticle dispersion behavior in the molten state. Practical deployment also requires stable large-scale nanoparticle dispersion and verification of compatibility with pumping and circulation systems. Accordingly, future studies should focus on the scalable preparation and dispersion processes for V_O-SiO_2 nanoparticles, establish cost-assessment models under industrially relevant production conditions, and evaluate their dispersion stability, flow behavior, and system compatibility under more realistic operating conditions. These efforts will facilitate the further development and practical application of defect-engineered molten-salt nanofluids.

4 | Method

4.1 | Materials and Sample Preparation

Solar salt was prepared by mixing $NaNO_3$ and KNO_3 at a mass ratio of 60:40. To introduce V_O, untreated SiO_2 nanoparticles were annealed at 1150°C for 5 or 8 h under an N_2 atmosphere in a tube furnace (GSL-1700X, Hefei Kejing Materials Technology Co., Ltd., China), followed by natural cooling under N_2. The untreated or V_O-engineered SiO_2 nanoparticles were then mixed with solar salt at a fixed nanoparticle mass fraction of 1 wt.%. The mixtures were ground at 200 rpm for 10 min using a planetary ball mill (QM-3SP04, Zhengxian, Nanjing Nanda Instrument Co., Ltd., China) to uniformly disperse the nanoparticles in the base salt. The nanofluid containing untreated SiO_2 nanoparticles was denoted as MSNF, while those containing V_O-engineered SiO_2 nanoparticles annealed for 5 and 8 h were denoted as V_O-MSNF-5h and V_O-MSNF-8h, respectively.

4.2 | EPR Measurement

EPR measurements were performed at room temperature using an X-band spectrometer (EMXplus-6/1, Bruker, Germany) operating in continuous-wave mode. The microwave frequency was approximately 9.84 GHz. Powder samples were sealed in quartz tubes and positioned at the center of the cavity. The spectra were recorded in the first-derivative mode with a central field of 3505 G, a sweep width of 100 G, a microwave power of 3.2 mW, a modulation amplitude of 3.0 G, a modulation frequency of 100 kHz, and five accumulations. The data were baseline-corrected and normalized using Bruker software.

4.3 | DSC/TG Measurements

DSC was simultaneously measured by DSC 2500, TA Instruments, USA, and the equivalent values of melting point, melting latent heat, and c_p were obtained. During the test, a platinum crucible was used to hold the sample over sampling intervals of 1 s. The measurement was carried out in the following procedure: the temperature was first kept at a constant of 25°C for 10 min to stabilize the DSC signal and then increased to 500°C at a heating rate of 20°C min^{-1}. Nitrogen was used as the shielding gas, and a sapphire standard sample was used for the specific heat testing and calibration. Through the measured heat flow values of the sample and sapphire standard sample, the values of c_p of the base salt and nanofluids were obtained by the comparison method. For each composition, the specific heat capacity measurement was performed three times under identical conditions. The calculation formula is as follows [50]:

$$c_{p,sample} = c_{p,sapphire} \cdot \frac{DSC_{sample} - DSC_{baseline}}{DSC_{sapphire} - DSC_{baseline}} \quad (1)$$

where $c_{p,\,sample}$ and $c_{p,\,sapphire}$ are the specific heat capacity values of the sample, sapphire, respectively, and the unit of c_p is J g^{-1} K^{-1}; DSC_{sample}, $DSC_{sapphire}$, and $DSC_{baseline}$ are the DSC values of the sample, sapphire, and baseline, respectively, and the unit of DSC is W g^{-1}.

16146840, 2026, 40, Downloaded from https://advanced.onlinelibrary.wiley.com/doi/10.1002/aenm.71588 by Bingyang Cao - Tsinghua University Library , Wiley Online Library on [28/10/2026]. See the Terms and Conditions (https://onlinelibrary.wiley.com/terms-and-conditions) on Wiley Online Library for rules of use; OA articles are governed by the applicable Creative Commons License

TG measurements were conducted using a simultaneous thermal analyzer (STA PT 1600, LINSEIS, Germany) under an N_2 atmosphere.

4.4 | Thermal Conductivity Measurement

The thermal diffusivity of the samples was measured using a laser flash apparatus (LFA 467, NETZSCH, Germany) under an N_2 atmosphere. Disk-shaped specimens with a diameter of 14.8 mm and a thickness of 1.7 mm were tested using a three-layer configuration, where the sample was sandwiched between two stainless steel 310 reference layers. A short laser pulse was applied to the front surface, and the temperature rise on the rear surface was detected by an HgCdTe (MCT) infrared detector to determine the thermal diffusivity. The thermal conductivity was calculated below:

$$\lambda = \alpha \rho c_p \tag{2}$$

where α is the thermal diffusivity, ρ is the density, and c_p is the specific heat capacity.

4.5 | Rheological Measurements

The viscosities of solar salt, MSNF, and V_O-MSNF were measured in the molten state using a rotational rheometer (DHR-2, TA Instruments, USA). The samples were tested at 300°C, 350°C, 400°C, and 450°C under steady-shear conditions at a shear rate of 200 s^{-1}. During the measurements, rotational deformation was applied through the measuring system, and the resulting torque and rotational response were recorded by the instrument to determine the viscosity. The measurements at different temperatures were used to characterize the temperature dependence of viscosity and compare the flow behavior of the three molten salt systems. The viscosity was calculated from the measured shear stress according to $\eta = \tau/\gamma$, where η is the viscosity, τ is the shear stress, and γ is the shear rate.

4.6 | DFT Calculations and MD Simulations

The SiO_2 crystal structure was first expanded into a supercell using Atomsk software [51], from which a spherical nanoparticle with a radius of 7.5 Å was extracted. The resulting nanoparticle had an approximate diameter of 15 Å and a nominal spherical surface area of approximately 707 $Å^2$ contained 40 Si atoms and 80 O atoms. Subsequently, 20 O atoms were selectively removed from the surface of the nanoparticle to create a defect structure with 20 V_O. The total number of atoms in the nanoparticle was 100. The geometric optimization and charge calculation of the above structure were performed using the $DMol^3$ module [52] in the Materials Studio software. The B3LYP functional and DNP basis [53] set were used during the optimization, with energy convergence set to 2×10^{-5} Ha, gradient convergence to 0.004 Ha/Å, and the maximum displacement to 0.05 Å. The system's charge was adjusted to 20 e based on the number of V_O [54], and the spin polarization was unconstrained. The V_O concentration in the MD model was used to qualitatively investigate the defect-induced interfacial mechanism rather than to reproduce the absolute oxygen-vacancy concentration in the experimental sample.

MD simulations have been widely used to predict molten-salt thermophysical properties [55]. The solar salt system contained 1676 $NaNO_3$ and 941 KNO_3 molecules, corresponding to 13085 molten-salt atoms and a $NaNO_3/KNO_3$ mass ratio of approximately 60:40. The single-particle MSNF and V_O-MSNF systems contained one nanoparticle and 13205 and 13185 atoms, respectively, with the nanoparticle loading fixed at 1 wt.%. Dual-particle models containing two nanoparticles were additionally constructed for the dispersion analysis. The detailed compositions of all simulation systems are summarized in Table S5. The interactions within solar salt and SiO_2 were described using Buckingham potentials with Coulombic interactions. The N-O bond and O-N-O angle interactions within NO_3^- were represented by harmonic and CHARMM potentials, respectively, whereas the interactions between the molten-salt ions and SiO_2 nanoparticles were described using Lennard-Jones and Coulombic interactions. The corresponding potential parameters and Lorentz-Berthelot mixing rules are provided in Tables S6–S8.

A cubic simulation box was employed with periodic boundary conditions applied to eliminate the boundary effects. A cutoff radius of 15 Å was used for the calculations of c_p and thermal conductivity, while a cutoff radius of 25 Å was applied for the analysis of nanoparticle dispersion. Long-range Coulombic interactions were treated using the Ewald summation method [15] with a precision of 1×10^{-4}. The initial velocities were randomly assigned according to a Gaussian distribution. The equations of motion were integrated using the Verlet algorithm [56] with a timestep of 0.5 fs. The system was first annealed under the isothermal-isobaric ensemble (NPT) by heating from 273 to 823 K and then cooling to the target temperature. After annealing, equilibration was carried out for 0.5 ns under both the NPT and canonical (NVT) ensembles at the target temperature. For the calculation of c_p, the NVT ensemble was employed for 1 ns, whereas for the calculation of thermal conductivity, the microcanonical (NVE) ensemble was adopted for 1 ns. The specific heat capacity was calculated using the energy-fluctuation method, whereas the thermal conductivity was determined using the RNEMD method, as described by Equations S9 and S10, respectively.

4.7 | CSP Techno-Economic Modeling

The techno-economic performance of CSP systems using solar salt, MSNF, and V_O-MSNF as the TES medium was evaluated using the SAM [49]. Three system configurations were considered: PTC-RC, SPT-BC, and SPT-RC. The heliostat field of the SPT systems was generated using DELSOL3, and the cycle thermal efficiencies were calculated using the NREL Python program. An SM of 2 and a TES hour of 6 h were adopted for the baseline comparison. Two design conditions were considered: fixed thermal capacity and fixed storage volume. The thermophysical properties and costs of the three TES media were incorporated into the corresponding SAM models, while the main technical, financial, and operating assumptions, including plant lifetime, inflation rate, degradation rate, and operation and maintenance costs, are summarized in Tables S10–S13. The TES-medium and

16146840, 2026, 40, Downloaded from https://advanced.onlinelibrary.wiley.com/doi/10.1002/aenm.71588 by Bingyang Cao - Tsinghua University Library , Wiley Online Library on [28/10/2026]. See the Terms and Conditions (https://onlinelibrary.wiley.com/terms-and-conditions) on Wiley Online Library for rules of use; OA articles are governed by the applicable Creative Commons License

storage-device costs were calculated based on the material requirement and storage volume, with the detailed cost assumptions provided in Table S3.

Author Contributions

C.J.: Conceptualization, methodology, data curation, investigation, formal analysis, Writing – original draft. **X.Y.:** Conceptualization, investigation, formal analysis, supervision, funding acquisition, resources, Writing – original draft. **Q.C.:** Formal analysis, validation. **X.Z.:** Investigation, supervision. **J.X.:** Supervision. **B.C.:** Writing – original draft, supervision, funding acquisition. All authors contributed to writing, review, and editing and approved the final version of the manuscript.

Acknowledgements

This work was financially supported by the National Natural Science Foundation of China under Grant No. 52425601, the Natural Science Foundation of Hebei Province of China under Grant No. E2025502029, and the Beijing Municipal Science & Technology Commission and Administrative Commission of Zhongguancun Science Park under Grant No. Z251100003625023.

Conflicts of Interest

The authors declare no conflicts of Interest.

Data Availability Statement

The data that support the findings of this study are available from the corresponding author upon reasonable request.

References

1. S. Saher, S. Johnston, R. Esther-Kelvin, J. M. Pringle, D. R. MacFarlane, and K. Matuszek, "Trimodal Thermal Energy Storage Material for Renewable Energy Applications," *Nature* 636, no. 8043 (2024): 622–626, https://doi.org/10.1038/s41586-024-08214-1.

2. S. J. Davis, N. S. Lewis, and M. Shaner, et al., "Net-Zero Emissions Energy Systems," *Science* 360, no. 6396 (2018): aas9793, https://doi.org/10.1126/science.aas9793.

3. T. Levin, J. Bistline, R. Sioshansi, et al., "Energy Storage Solutions to Decarbonize Electricity Through Enhanced Capacity Expansion Modelling," *Nature Energy* 8, no. 11 (2023): 1199–1208, https://doi.org/10.1038/s41560-023-01340-6.

4. N. S. Lewis, "Research Opportunities to Advance Solar Energy Utilization," *Science* 351, no. 6271 (2016): aad1920, https://doi.org/10.1126/science.aad1920.

5. L. Duan, R. Petroski, L. Wood, and K. Caldeira, "Stylized Least-Cost Analysis of Flexible Nuclear Power in Deeply Decarbonized Electricity Systems Considering Wind and Solar Resources Worldwide," *Nature Energy* 7, no. 3 (2022): 260–269, https://doi.org/10.1038/s41560-022-00979-x.

6. C. Shen, S. Attarian, Y. Zhang, et al., "Supersalt: Equivariant Neural Network Force Fields for Multicomponent Molten Salts System," *Nature Communications* 16, no. 1 (2025): 7280, https://doi.org/10.1038/s41467-025-62450-1.

7. Y. Wang, Y. Lu, Y. Wu, and C. Zhang, "Phase Diagram Analysis and Thermophysical Properties Investigation of Mixed Molten Salts With Low Liquid Operating Temperature for Thermal Energy Storage," *Energy* 333, (2025): 137386, https://www.sciencedirect.com/science/article/pii/S0360544225030282.

8. Z. An, S. Mao, X. Du, D. Zhang, J. Fu, and Y. Ding, "In-Depth Molecular Dynamics Analysis of the Thermal Energy Storage and Transfer Enhancement Mechanism Within Carbonate Nanofluid System," *International Journal of Heat and Mass Transfer* 255 (2026): 127825, https://www.sciencedirect.com/science/article/pii/S0017931025011603.

9. X. Jin and X. Xiao, "Molecular Dynamics Simulation of the Effects of SiO_2 Nanoparticles on Thermophysical Properties of Low Concentration Salt Solution Fluid," *International Journal of Heat and Mass Transfer* 255 (2026): 127816, https://www.sciencedirect.com/science/article/pii/S0017931025011512.

10. Q. Luo, X. Liu, Q. Xu, et al., "Ceramic Nanoparticles Enhancement of Latent Heat Thermal Energy Storage Properties for $LiNO_3$/NaCl: Evaluation From Material to System Level," *Applied Energy* 331 (2023): 120418, https://www.sciencedirect.com/science/article/pii/S0306261922016750.

11. C. Ji, X. Yang, H. Xu, J. Lai, and J. Xie, "Advances in Molten Salt-Based Nanofluids: Thermal Property Enhancement and Applications in CSP and Power Systems," *Renewable and Sustainable Energy Reviews* 226 (2026): 116360, https://www.sciencedirect.com/science/article/pii/S1364032125010330.

12. M. Yao and X. Xiao, "Advance of Molecular Dynamics Simulations in the Thermophysical Properties of Molten Salts: A Critical Review," *Renewable and Sustainable Energy Reviews* 229 (2026): 116609, https://www.sciencedirect.com/science/article/pii/S1364032125012821.

13. U. Nithiyanantham, A. Zaki, Y. Grosu, et al., "Effect of Silica Nanoparticle Size on the Stability and Thermophysical Properties of Molten Salts Based Nanofluids for Thermal Energy Storage Applications at Concentrated Solar Power Plants," *Journal of Energy Storage* 51 (2022): 104276, https://www.sciencedirect.com/science/article/pii/S2352152.

14. B. Jo and D. Banerjee, "Viscosity Measurements of Multi-Walled Carbon Nanotubes-Based High Temperature Nanofluids," *Materials Letters* 122 (2014): 212–215, https://www.sciencedirect.com/science/article/pii/S0167577.

15. L. Xian, L. Chen, H. Tian, and W. Tao, "Enhanced Thermal Energy Storage Performance of Molten Salt for the Next Generation Concentrated Solar Power Plants by SiO_2 Nanoparticles: A Molecular Dynamics Study," *Applied Energy* 323 (2022): 119555, https://www.sciencedirect.com/science/article/pii/S0306261922008686.

16. J. Liu and X. Xiao, "Molecular Dynamics Investigation of Thermo-Physical Properties of Molten Salt With Nanoparticles for Solar Energy Application," *Energy* 282, (2023): 128732, https://www.sciencedirect.com/science/article/pii/S0360544223021266.

17. F. Yuan, M. Li, Y. Qiu, Z. Ma, and M. Li, "Specific Heat Capacity Improvement of Molten Salt for Solar Energy Applications Using Charged Single-Walled Carbon Nanotubes," *Applied Energy* 250 (2019): 1481–1490, https://www.sciencedirect.com/science/article/pii/S030626191930827X.

18. C. Ji, X. Yang, H. Xu, Z. Yang, and J. Xie, "Molecular Insight Into Further Enhancement of Thermal Conductivity and Heat Capacity of K_2CO_3-SiO_2 Molten Salt Nanofluids by Oxygen Vacancy Defects in SiO_2 Nanoparticles," *International Journal of Heat and Mass Transfer* 247 (2025): 127148, https://www.sciencedirect.com/science/article/pii/S0017931025004879.

19. H. R. Wen, S. C. Lin, C. Y. Zhao, and E. L. Wang, "Nanoparticle Surface Charge-Enhanced Heat Capacity in Molten Salt Phase Change Materials for Thermal Energy Storage," *Solar Energy Materials and Solar Cells* 243 (20222): 111795, https://www.sciencedirect.com/science/article/pii/S092702482200215X.

20. V. V. Potapov and L. T. Zhuravlev, "Temperature Dependence of the Concentration of Silanol Groups in Silica Precipitated From a Hydrothermal Solution," *Glass Physics and Chemistry* 31, no. 5 (2005): 661–670, https://doi.org/10.1007/s10720-005-0111-z.

21. M. Walters and A. Reisman, "Distribution Phenomena of Charged Defects and Neutral Electron Traps in Process-Induced Radiation-Damaged IGFETs With Gate Insulators Grown at 1000 Degrees C and 800 Degrees C," (1990): 125–131, https://ieeexplore.ieee.org/document/66075.

22. E. V. Ivanova, A. A. Sitnikova, O. V. Aleksandrov, and M. V. Zamoryanskaya, "Growth of Silicon Nanoclusters in Thermal Silicon

16146840, 2026, 40, Downloaded from https://advanced.onlinelibrary.wiley.com/doi/10.1002/aenm.71588 by Bingyang Cao - Tsinghua University Library , Wiley Online Library on [28/10/2026]. See the Terms and Conditions (https://onlinelibrary.wiley.com/terms-and-conditions) on Wiley Online Library for rules of use; OA articles are governed by the applicable Creative Commons License

Dioxide Under Annealing in an Atmosphere of Nitrogen," *Semiconductors* 50, no. 6 (2016): 791–794, https://doi.org/10.1134/S1063782616060099.

23. E. V. Ivanova, P. A. Dementev, A. A. Sitnikova, O. V. Aleksandrov, and M. V. Zamoryanskaya, "High-Temperature Annealing as a Method for the Silicon Nanoclusters Growth in Stoichiometric Silicon Dioxide," *Journal of Electronic Materials* 47, no. 7 (2018): 3969–3973, https://doi.org/10.1007/s11664-018-6280-z.

24. K. Clémer, A. Stesmans, and V. V. Afanas'Ev, "Electron Spin Resonance Probing of E′-Type Defects in Fumed Silica Nanoparticles," *Materials Science and Engineering: C* 26, no. 5 (2006): 766–770, https://www.sciencedirect.com/science/article/pii/S0928493105002419.

25. A. Datas, A. López-Ceballos, E. López, A. Ramos, and C. Del Cañizo, "Latent Heat Thermophotovoltaic Batteries," *Joule* 6, no. 2 (2022): 418–443, https://www.sciencedirect.com/science/article/pii/S2542435122000423.

26. P. Andreu-Cabedo, R. Mondragon, L. Hernandez, R. Martinez-Cuenca, L. Cabedo, and J. E. Julia, "Increment of Specific Heat Capacity of Solar Salt With SiO_2 Nanoparticles," *Nanoscale Research Letters* 9, no. 1 (2014): 582, https://doi.org/10.1186/1556-276X-9-582.

27. B. Dudda and D. Shin, "Effect of Nanoparticle Dispersion on Specific Heat Capacity of a Binary Nitrate Salt Eutectic for Concentrated Solar Power Applications," *International Journal of Thermal Sciences* 69 (2013): 37–42, https://www.sciencedirect.com/science/article/pii/S1290072913000367.

28. J. Seo and D. Shin, "Size Effect of Nanoparticle on Specific Heat in a Ternary Nitrate ($LiNO_3$–$NaNO_3$–KNO_3) Salt Eutectic for Thermal Energy Storage," *Applied Thermal Engineering* 102 (2016): 144–148, https://www.sciencedirect.com/science/article/pii/S1359431116304422.

29. Z. Han, M. K. Ram, R. Kamal, T. Alamro, D. Y. Goswami, and C. Jotshi, "Characterization of Molten Salt Doped With Different Size Nanoparticles of Al_2O_3," *International Journal of Energy Research* 43, no. 8 (2019): 3732–3745, https://doi.org/10.1002/er.4531.

30. Y. Luo, X. Du, A. Awad, and D. Wen, "Thermal Energy Storage Enhancement of a Binary Molten Salt Via in-Situ Produced Nanoparticles," *International Journal of Heat and Mass Transfer* 104 (2017): 658–664, https://www.sciencedirect.com/science/article/pii/S0017931016313400.

31. M. Liu, J. Severino, F. Bruno, and P. Majewski, "Experimental Investigation of Specific Heat Capacity Improvement of a Binary Nitrate Salt by Addition of Nanoparticles/Microparticles," *Journal of Energy Storage* 22 (2019): 137–143, https://www.sciencedirect.com/science/article/pii/S2352152X1830584X.

32. C. Zhang, M. F. Calegari Andrade, Z. K. Goldsmith, et al., "Molecular-Scale Insights Into the Electrical Double Layer at Oxide-Electrolyte Interfaces," *Nature Communications* 15, no. 1 (2024): 10270, https://doi.org/10.1038/s41467-024-54631-1.

33. X. Mao, P. Brown, C. Cervinka, et al., "Self-Assembled Nanostructures in Ionic Liquids Facilitate Charge Storage at Electrified Interfaces," *Nature Materials* 18, no. 12 (2019): 1350–1357, https://doi.org/10.1038/s41563-019-0449-6.

34. B. Nouwen, V. V. Afanas Ev, and A. Stesmans, "Structural Degradation of Thermal SiO_2 on Si by High-Temperature Annealing: Defect Generation," *Physical Review B* 66, no. 4 (2002): 45307, https://link.aps.org/doi/10.1103/PhysRevB.66.045307.

35. M. Senna, H. Noda, Y. Xin, et al., "Solid-State Reduction of Silica Nanoparticles Via Oxygen Abstraction From SiO_4 Units by Polyolefins Under Mechanical Stressing," *RSC Advances* 8, no. 63 (2018): 36338–36344, https://doi.org/10.1039/c8ra07271j.

36. Y. Hu, Y. He, Z. Zhang, and D. Wen, "Enhanced Heat Capacity of Binary Nitrate Eutectic Salt-Silica Nanofluid for Solar Energy Storage," *Solar Energy Materials and Solar Cells* 192 (2019): 94–102, https://www.sciencedirect.com/science/article/pii/S0927024818305877.

37. M. Betts, *The Effects of Nanoparticle Augmentation of Nitrate Thermal Storage Materials for Use in Concentrating Solar Power Applications* 2011, 18–22.

38. Z. Li, L. Cui, B. Li, and X. Du, "Effects of SiO_2 Nanoparticle Dispersion on the Heat Storage Property of the Solar Salt for Solar Power Applications," *Energies* 14, no. 3 (2021): 703, https://www.mdpi.com/1996-1073/14/3/703.

39. C. Cockrell, M. Withington, H. L. Devereux, et al., "Thermodynamics and Transport in Molten Chloride Salts and their Mixtures," *Physical Chemistry Chemical Physics* 27, no. 3 (2024): 1604–1615, https://doi.org/10.1039/d4cp04180a.

40. G. Qiao, A. Alexiadis, and Y. Ding, "Simulation Study of Anomalous Thermal Properties of Molten Nitrate Salt," *Powder Technology* 314 (2017): 660–664, https://www.sciencedirect.com/science/article/pii/S0032591016307951.

41. A. Svobodova-Sedlackova, C. Barreneche, G. Alonso, A. I. Fernandez, and P. Gamallo, "Effect of Nanoparticles in Molten Salts—MD Simulations and Experimental Study," *Renewable Energy* 152 (2020): 208–216, https://www.sciencedirect.com/science/article/pii/S0960148120300513.

42. Z. Li, L. Cui, B. Li, and X. Du, "Mechanism Exploration of the Enhancement of Thermal Energy Storage in Molten Salt Nanofluid," *Physical Chemistry Chemical Physics* 23, no. 23 (2021): 13181–13189, https://doi.org/10.1039/D1CP00125F.

43. C. Yan, J. Liang, X. Zhong, et al., "BN White Graphene Well-Dispersed Solar Salt Nanofluids With Significant Improved Thermal Properties for Concentrated Solar Power Plants," *Solar Energy Materials and Solar Cells* 245 (2022): 111875, https://www.sciencedirect.com/science/article/pii/S0927024822002951.

44. L. Sang, W. Ai, Y. Wu, and C. Ma, "Enhanced Specific Heat and Thermal Conductivity of Ternary Carbonate Nanofluids With Carbon Nanotubes for Solar Power Applications," *International Journal of Energy Research* 44, no. 1 (2019): 334–343, https://doi.org/10.1002/er.4923.

45. R. Serrano-López, J. Fradera, and S. Cuesta-López, "Molten Salts Database for Energy Applications," *Chemical Engineering and Processing: Process Intensification* 73 (2013): 87–102, https://www.sciencedirect.com/science/article/pii/S0255270113001827.

46. C. Cockrell, M. Withington, H. L. Devereux, et al., "Thermal Conductivity and Thermal Diffusivity of Molten Salts: Insights From Molecular Dynamics Simulations and Fundamental Bounds," *The Journal of Physical Chemistry B* 129, no. 8 (2025): 2271–2279, https://doi.org/10.1021/acs.jpcb.4c07565.

47. H. Matsubara, G. Kikugawa, T. Bessho, S. Yamashita, and T. Ohara, "Molecular Dynamics Study on the Role of Hydroxyl Groups in Heat Conduction in Liquid Alcohols," *International Journal of Heat and Mass Transfer* 108 (2017): 749–759, https://www.sciencedirect.com/science/article/pii/S0017931016328940.

48. L. Wang, F. Zhao, H. Yu, R. Xia, Z. Jiang, and W. Feng, "Graphene Oxide-Molten Salt Composite Material for High-Temperature Photothermal Phase Change Energy Storage," *Advanced Functional Materials* 36, no. 46 (2026): 75374, https://doi.org/10.1002/adfm.75374.

49. N. Blair, A. P. Dobos, and J. Freeman, et al., "System Advisor Model, SAM 2014.1.14: General Description," Technical Report NREL/TP-6A20-61019 (National Renewable Energy Laboratory, 2014), https://doi.org/10.2172/1126294.

50. X. Yang, W. Jiang, C. Ji, and Q. Wang, "Experimental Study on Heat Storage and Corrosion Properties of Ternary Carbonate Salt-Based ZnO Nanofluids for Solar Thermal Energy Storage," *Journal of Thermal Analysis and Calorimetry* 147, no. 23 (2022): 13935–13947, https://doi.org/10.1007/s10973-022-11654-4.

51. P. Hirel, "Atomsk: A Tool for Manipulating and Converting Atomic Data Files," *Computer Physics Communications* 197 (2015): 212–219, https://www.sciencedirect.com/science/article/pii/S0010465515002817.

52. B. Delley, "From Molecules to Solids With the $Dmol^3$ Approach," *The Journal of Chemical Physics* 113, no. 18 (2000): 7756–7764, https://doi.org/10.1063/1.1316015.

16146840, 2026, 40, Downloaded from https://advanced.onlinelibrary.wiley.com/doi/10.1002/aenm.71588 by Bingyang Cao - Tsinghua University Library , Wiley Online Library on [28/10/2026]. See the Terms and Conditions (https://onlinelibrary.wiley.com/terms-and-conditions) on Wiley Online Library for rules of use; OA articles are governed by the applicable Creative Commons License

53. K. Burke, M. Ernzerhof, and J. P. Perdew, "Generalized Gradient Approximation Made Simple," *Physical Review Letters* 77, no. 18 (1996): 3865–3868, https://link.aps.org/doi/10.1103/PhysRevLett.77.3865.

54. M. S. Munde, D. Z. Gao, and A. L. Shluger, "Diffusion and Aggregation of Oxygen Vacancies in Amorphous Silica," *Journal of Physics: Condensed Matter* 29, no. 24 (2017): 245701, https://doi.org/10.1088/1361-648X/aa6f9a.

55. T. Porter, M. M. Vaka, P. Steenblik, and D. Della Corte, "Computational Methods to Simulate Molten Salt Thermophysical Properties," *Communications Chemistry* 5, no. 1 (2022): 69, https://doi.org/10.1038/s42004-022-00684-6.

56. M. P. Allen and D. J. Tildesley, *Computer Simulation of Liquids* (Oxford University Press, 2017), https://doi.org/10.1093/oso/9780198803195.001.0001.

Supporting Information

Additional supporting information can be found online in the Supporting Information section.

Supporting File: aenm71588-sup-0001-SuppMat.docx.

16146840, 2026, 40, Downloaded from https://advanced.onlinelibrary.wiley.com/doi/10.1002/aenm.71588 by Binglyang Cao - Tsinghua University Library , Wiley Online Library on [28/10/2026]. See the Terms and Conditions (https://onlinelibrary.wiley.com/terms-and-conditions) on Wiley Online Library for rules of use; OA articles are governed by the applicable Creative Commons License